ORIGINAL PAPER

Mixed-dimensional multi-scale poroelastic modeling of adipose tissue for subcutaneous injection

Yu Leng[1] · Hao Wang[1] · Mario de Lucio[1] · Hector Gomez[1]

Abstract

Subcutaneous injection of therapeutic monoclonal antibodies (mAbs) has gained increasing interest in the pharmaceutical industry. The transport, distribution and absorption of mAbs in the skin after injection are not yet well-understood.Experiments have shown that fibrous septa form preferential channels for fluid flow in the tissue.The majority of mAbs can only be absorbed through lymphatics which follow closely the septa network.Therefore, studying drug transport in the septa network is vital to the understanding of drug absorption.In this work, we present a mixed-dimensional multi-scale (MDMS) poroelastic model of adipose tissue for subcutaneous injection.More specifically, we model the fibrous septa as reduced-dimensional microscale interfaces embedded in the macroscale tissue matrix.The model is first verified by comparing numerical results against the full-dimensional model where fibrous septa are resolved using fine meshes.Then, we apply the MDMS model to study subcutaneous injection. It is found that the permeability ratio between the septaand matrix, volume capacity of the septa network, and concentration-dependent drug viscosity are important factors affecting the amount of drug entering the septa network which are paths to lymphatics.Our results show that septa play a critical role in the transport of mAbs in the subcutaneous tissue, and this role was previously overlooked.

Keywords Subcutaneous injection · Mixed-dimensional multi-scale modeling · Poroelasticity · Fibrous septa · Adipose tissue · Drug transport

1 Introduction

The treatment of many diseases (Lu et al. 2020),such as migranies (Tso and Goadsby 2017), cancers (Glassman and Balthasar 2014; Pivot et al. 2014), psoriasis (Burmester et al. 2013), and COVID-19 (Taylor et al. 2021), relies on effective delivery of therapeutic antibodies (mAbs).Subcutaneous delivery of mAbs has attracted increasing attention in the pharmaceutical and healthcare industries due to its increased patient compliance and convenience as well as reduced healthcare expenses (Haller 2007; Jackisch et al. 2014). However, compared to intravenous administration, further development of subcutaneous delivery is hindered by many challenges including low bioavalibility (Bittner et al. 2018; Porter et al. 2001) and limited deliverable volume (Jackisch et al. 2014; Shpilberg and Jackisch 2013).To overcome these

challenges and to improve delivery strategies, the study of drug transport and distribution in the adipose tissue during and after administration becomes critical.

A histological image of porcine adipose tissue is shown in Fig. 1a.Adipose tissue consists of adipocytes, collagen fibers, blood and lymphatic capillaries (Comley and Fleck 2010).Lymphatic capillaries in the adipose tissue follow the fibrous septa (Klein 2000) which are bundles of collagen fibers (Comley and Fleck 2010).Due to their large molecular weight, mAbs are primarily absorbed by the lymphatic vessels and then enter the circulatory system (Hossain et al. 2013; Porter and Charman 2000; Supersaxo et al. 1990; Thomas and Balthasar 2019; Wang et al. 2012; Zhao et al. 2013).The convoluted route of mAbs entering the blood system is one of the reasons for their low bioavailability upon subcutaneous delivery. It is of high economic and scientific interest to study the transport and distribution of mAbs in adipose tissue after injection.Fibers are prelymphatic pathways for drug transport because their flow resistance is low (Ryan 1989; Skobe and Detmar 2000).As shown in Fig. 1b, septa form preferential channels for fluid flow (Thomsen

✉ Yu Leng
  leng10@purdue.edu

1 School of Mechanical Engineering, Purdue University,
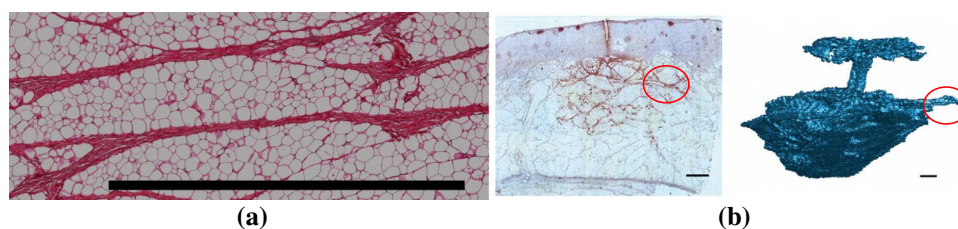   West Lafayette, IN 47907, USA

(a)   **(b)**

Fig. 1 **a** Histological image of porcine adipose tissue. Adipocytes are shown in white. The septa are shown as magenta stripes. The scale bar is 1.5 mm. **b** Subcutaneous injection experiments, taken from Thomsen et al. (2014). (Left) Histological cross section. The drug has been dyed to appear red. (Right) X-ray CT scan of a similar injection. The volume shows the 3D shape of the drug plume. Preferential channels for fluid flow along septa are circled in red. The scale bar is 1 mm

et al. 2014). Therapeutic proteins (mAbs), entering the septa network, are in close contact with the lymphatics, thus are more likely to be absorbed before undergoing catabolism (Porter et al. 2001; Thomas and Balthasar 2019). As shown in Fig. 1a, there is a rich network of septa in adipose tissue. The diameter of septa bundles ranges from 30 µm to 10 nm for porcine tissue (Comley and Fleck 2010), and the maximum thickness can be as large as several hundred microns in healthy non-cellulite human adipose tissue (Hexsel et al. 2009; Macchi et al. 2010; Wang et al. 2011). The contrast between the septa width and the characteristic length scales for tissue deformation and drug transport make this a multiscale problem. Thus, we will consider septa as microscale features embedded in a macroscale tissue. The goal of this work is to model fluid flow and drug transport in the mascroscale tissue and along the microscale septa. We aim to study the volume fraction of injected drug entering the septa network in the adipose tissue.

Previous works (Leng et al. 2021a, b; de Lucio et al. 2020) have modeled the adipose tissue as porous media to study the mechanical response and pressure build-up in the tissue due to injection. It was found that solid deformation is important in predicting pressure distribution, and thus drug transport during subcutaneous injection. Drug transport coupled with solid deformation is also considered in Han et al. (2021) and Rahimi et al. (2022). However, these studies (Han et al. 2021; Leng et al. 2021a, b; de Lucio et al. 2020; Rahimi et al. 2022; Weickenmeier and Mazza 2019) are limited to the macroscale tissue matrix, and fail to consider the microscale fibrous septa. Fibers in soft materials have been well-studied, and their homogeneous contributions to macroscale solid deformation are studied in NíAnnaidh et al. (2012) and Sommer et al. (2013). In subcutaneous injection, the role of septa as preferential channels for fluid flow is similar to that of natural fractures in geophysical flows. Discrete fractures-matrix models are popular in modeling fluid flow in fractured porous media (Alboin et al. 2000; Angot et al. 2009; Faille et al. 2016; Flemisch et al. 2018; Frih et al. 2012; Froeschl 2003; Fumagalli and Scotti 2013; Martin et al. 2005; Odsæter et al. 2019; Schädle et al. 2019;

Schwenck et al. 2015). The governing equations are averaged across the fractures, thus fractures can be represented as lower-dimensional interfaces embedded in the matrix. We borrow ideas from discrete fracture-matrix models and include the fibrous septa as interfaces in the adipose tissue matrix.

In this work, we present a mixed-dimensional multi-scale (MDMS) poroelastic model of the adipose tissue for subcutaneous injection. The macroscale tissue matrix is modeled as a deformable porous media. The fibrous septa are considered as reduced-dimensional microscale interfaces embedded in the tissue matrix. The solid deformation of the septa is homogeneous and characterized by the macroscale matrix. The fluid flow and drug transport along the septa are modeled explicitly. The model is first verified by comparing numerical results against the full two-dimensional (2D) model where fibrous septa are resolved using fine meshes. Then, we apply the MDMS model to study subcutaneous injection of mAbs. We investigate model parameters that contribute significantly to volume of drug entering the septa network which are paths to lymphatics. Our results show that septa play a critical role in the transport of mAbs in the subcutaneous tissue.

This paper is organized as follows. Section 2 introduces the MDMS poroelastic model. Numerical methods are discussed in Sect. 3. The MDMS poroelastic model is verified in Sect. 4, and is applied to study subcutaneous injection in Sect. 5. Finally, Sect. 6 summarizes the findings of this work.

2 Model equations

In this section, we present the MDMS poroelastic model for the adipose tissue. The tissue matrix is modeled using the full-dimensional poroelastic model with drug transport in the tissue matrix. The septa are modeled using a reduced-dimension model.

We introduce first some notations that are used throughout the rest of the paper. Let $\Omega \subset \mathbb{R}^d$, where $d = 2, 3$ is the spatial dimension, be an open and bounded domain with Lipschitz boundary $\partial\Omega$. Let $\Gamma \subset \mathbb{R}^{d-1}$ be a co-dimension one

subspace of Ω. The domain of the tissue matrix is represented by Ω, while Γ is the septa interface embedded in the matrix. Denote time as $t \in (0, T]$, where $T > 0$ is the time when the injection ends.

2.1 Full-dimensional model for the tissue

The poroelastic model (Biot 1941, 1956; Biot and Temple 1972) with fluid transport (Kadeethum et al. 2021; Rudraraju et al. 2013; Tran and Jha 2020), is used to model the adipose tissue. We assume that the mechanical response of the tissue matrix and fluid flow therein can becharacterized using the homogeneous macroscale poroelastic model. Under quasi-staticconditions and negligible gravitational effects (Biot 1941, 1956; Biot and Temple 1972; Coussy 2004; Fornells et al. 2007; Kadeethum et al. 2021; Tran and Jha 2020),the equation of linear momentum in the tissue matrix can be written as

$$\nabla \cdot \boldsymbol{\sigma}(\boldsymbol{u}, p) = \mathbf{0}, \text{ with } \boldsymbol{\sigma}(\boldsymbol{u}, p) = \boldsymbol{\sigma}^{\text{eff}}(\boldsymbol{u}) - \alpha p \mathbf{I},$$
$$\text{in } \Omega \times (0, T], \tag{1}$$

where $\boldsymbol{\sigma}$ and $\boldsymbol{\sigma}^{\text{eff}}$ are the total Cauchy stress and effective stress tensors, respectively, $\boldsymbol{u}$ is the solid displacement, p is the pore pressure, α is the Biot coefficient, and $\mathbf{I}$ is the $d \times d$ identity tensor. We assume the tissue deformation is small, thus the effective stress $\boldsymbol{\sigma}^{\text{eff}}$ can be linearized as,

$$\boldsymbol{\sigma}^{\text{eff}}(\boldsymbol{u}) = 2G\epsilon(\boldsymbol{u}) + \lambda(\nabla \cdot \boldsymbol{u})\mathbf{I}, \text{ with } \epsilon(\boldsymbol{u}) = \frac{1}{2}\left(\nabla \boldsymbol{u} + \nabla \boldsymbol{u}^T\right),$$

where G and λ are the Lamé coefficients, and ϵ is the symmetric linear elastic strain. The Biot coefficient is defined as

$$\alpha = 1 - \frac{K}{K_s}, \tag{2}$$

where K is the drained modulus of the tissue, and K_s is the bulk modulus of the solid constituent.

Then, the conservation of mass is given as

$$\frac{1}{M}\frac{\partial p}{\partial t} + \alpha\frac{\partial \epsilon_v}{\partial t} + \nabla \cdot \boldsymbol{w} = q_f, \text{ in } \Omega \times (0, T], \tag{3}$$

where M is the Biot modulus, $\epsilon_v := \text{tr}(\epsilon) = \nabla \cdot \boldsymbol{u}$ is the volumetric strain, q_f is the source term modeling fluid injection, and $\boldsymbol{w}$ is the Darcy velocity

$$\boldsymbol{w} = -\mathcal{K}_m \nabla p, \text{ with } \mathcal{K}_m = \frac{k_m}{\mu_f}. \tag{4}$$

Herein, $\mathcal{K}_m$ is the hydraulic conductivity of the matrix, k_m is the permeability of the matrix, μ_f is the viscosity of the fluid. The Biot modulus is given by

$$\frac{1}{M} = \phi_0 c_f + \frac{\alpha - \phi_0}{K_s}, \tag{5}$$

where ϕ_0 is the porosity in the undeformed tissue, and c_f is the fluid compressibility.

We proceed next with the governing equation for drug transport. Let c and $\widetilde{c}_0$ (mg/mL) be the concentration of mAbs in the tissue and the initial concentration of mAbs in the syringe, respectively. We use a dimensionless quantity $C = c/\widetilde{c}_0$ to represent the drug concentration in the tissue. Before injection, $C = 0$ everywhere in the tissue. During injection, $C = 1$ at the injection site. The advection--diffusion equation for drug transport is given by

$$\frac{\partial}{\partial t}(\phi C) + \nabla \cdot (\boldsymbol{w}C) + \nabla \cdot (\phi D \nabla C) = q_f, \text{ in } \Omega \times (0, T], \tag{6}$$

where ϕ is the current porosity, and D is the diffusion coefficient of mAbs inside the skin tissue. The current porosity ϕ is the key to couple solid deformation with drug transport. We follow (Kadeethum et al. 2021; Tran and Jha 2020) to calculate ϕ as

$$\phi = \phi_0 + \frac{1}{M}(p - p_0) + (\alpha - \phi_0)(\epsilon_v - \epsilon_{v,0}). \tag{7}$$

Therein, p_0 and $\epsilon_{v,0}$ are the initial pressure and volumetric strain, respectively.

Finally, we assume both fluid and solid constituents in the tissuematrix are incompressible, namely $c_f = 0$ and $K_s = \infty$. As a result, $1/M = 0$ and $\alpha = 1$. The diffusion coefficient of mAbs is in the order of 10^{-7} cm^2/s (Hung et al. 2019; Wright et al. 2018), while the injection velocity at the injection site is larger than 1.0 m/s (de Lucio et al. 2020). During the injection process, convection is the dominant drug transport mechanismcompared to diffusion. Therefore, we neglect the diffusion of mAbsby letting $D = 0$. In summary, we arrive at the following governingequations for the tissue matrix,

$$\nabla \cdot \left(\boldsymbol{\sigma}^{\text{eff}} - p\mathbf{I}\right) = \mathbf{0}, \quad \text{in } \Omega \times (0, T], \tag{8a}$$

$$\frac{\partial \epsilon_v}{\partial t} + \nabla \cdot \boldsymbol{w} = q_f, \quad \text{in } \Omega \times (0, T], \tag{8b}$$

$$\frac{\partial}{\partial t}(\phi C) + \nabla \cdot (\boldsymbol{w}C) = q_f, \quad \text{in } \Omega \times (0, T]. \tag{8c}$$

2.2 A reduced-dimension model for septa

As shown in Fig. 1b,septa fibers form preferential channels for fluid flow. For this reason, we model thefluid flow along the fibrous septa explicitly. We introduce more notations before presentingthe model. As shown in Fig. 2a, $\boldsymbol{n}_\Gamma$ is the

Fig. 2 **a** A bundle of septa $\Gamma \subset \mathbb{R}^{d-1}$ embedded in the tissue matrix $\Omega \subset \mathbb{R}^d$. **b** Partition of elements and element faces based on their intersection with septa

(a)   **(b)**
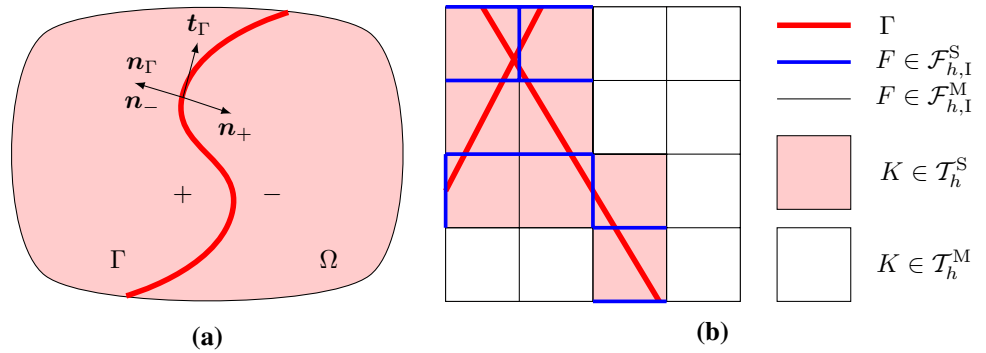
outward unit normal of Γ, and $\boldsymbol{t}_\Gamma$ is the unit vector in the tangential direction of Γ. For a scalar function φ, the jump across Γ is defined as

$$\llbracket \varphi \rrbracket = \varphi_+ - \varphi_-, \tag{9}$$

where

$$\begin{aligned} \varphi_+(\boldsymbol{x}) &= \lim_{\epsilon \to 0^+} \varphi(\boldsymbol{x} + \epsilon \boldsymbol{n}_\Gamma), \text{ and } \varphi_-(\boldsymbol{x}) \\ &= \lim_{\epsilon \to 0^+} \varphi(\boldsymbol{x} - \epsilon \boldsymbol{n}_\Gamma), \quad \boldsymbol{x} \in \Gamma. \end{aligned} \tag{10}$$

For a vector-valued function $\boldsymbol{v}$, the jump in the direction normal to Γ is defined by

$$\llbracket \boldsymbol{v} \cdot \boldsymbol{n} \rrbracket = \boldsymbol{v}_+ \cdot \boldsymbol{n}_+ + \boldsymbol{v}_- \cdot \boldsymbol{n}_-, \tag{11}$$

where $\boldsymbol{n}_+ = -\boldsymbol{n}_\Gamma$ and $\boldsymbol{n}_- = \boldsymbol{n}_\Gamma$.

We further assume that the fluid in the septa is incompressible, and that the deformation of the septa can be described by the deformation of the homogeneous tissue matrix. A reduced-dimension model, for fluid flow and transport along fractures that are embedded in rigid porous media, was proposed in Fumagalli and Scotti (2013) and Martin et al. (2005). We extend the model therein to describe fluid flow and drug transport in deformable porous tissue. The equation of conservation of mass along the septa is given as

$$\begin{cases} w_d \frac{\partial \epsilon_{v,\Gamma}}{\partial t} + \nabla_\Gamma \cdot \boldsymbol{w}_\Gamma = q_\Gamma + \llbracket \boldsymbol{w} \cdot \boldsymbol{n} \rrbracket, \\ \llbracket p \rrbracket = \hat{p}, \end{cases} \text{ on } \Gamma \times (0, T], \tag{12}$$

where w_d is the width of Γ, $\epsilon_{v,\Gamma} := \epsilon_v|_\Gamma$, $\nabla_\Gamma := \boldsymbol{P}\nabla$ is the tangential gradient and $\boldsymbol{P} = \left(\boldsymbol{I} - \boldsymbol{n}_\Gamma \otimes \boldsymbol{n}_\Gamma \right)$ is the tangential projection, q_Γ is the fluid injection inside the septa, $\hat{p}$ is the pressure jump across Γ, and $\boldsymbol{w}_\Gamma$ is the Darcy velocity along the septa. Herein, the Darcy velocity along the septa is defined similar to Eq. (4),

$$\boldsymbol{w}_\Gamma = -\mathcal{K}_\Gamma \nabla_\Gamma p, \text{ with } \mathcal{K}_\Gamma = \frac{k_\Gamma}{\mu_f} w_d, \tag{13}$$

where $\mathcal{K}_\Gamma$ and k_Γ are the hydraulic conductivity and permeability in the tangential direction of the septa, respectively. The last term in Eq. (12) models the fluid exchange between the tissue matrix and the septa.

Let C_Γ denote the dimensionless drug concentration inside the septa. The equation of drug transport along the septa (Fumagalli and Scotti 2013; Odsæter et al. 2019) is given by

$$w_d \frac{\partial}{\partial t}(\phi_\Gamma C_\Gamma) + \nabla_\Gamma \cdot \left(\boldsymbol{w}_\Gamma C_\Gamma \right) - \llbracket \boldsymbol{w} \cdot \boldsymbol{n} C^* \rrbracket = q_\Gamma,$$
$$\text{on } \Gamma \times (0, T], \tag{14}$$

where $\phi_\Gamma := \phi|_\Gamma$ is the current porosity in the septa, $\llbracket \boldsymbol{w} \cdot \boldsymbol{n} C^* \rrbracket$ is the drug concentration change between the tissue matrix and the septa, and C^* is the upwind concentration, defined as

$$C^* = \begin{cases} C_\pm, & \text{if } \boldsymbol{w}_\pm \cdot \boldsymbol{n}_\pm \geq 0, \\ C_\Gamma, & \text{otherwise,} \end{cases} \text{ on } \Gamma \times (0, T]. \tag{15}$$

We assume that the septa have a higher hydraulic conductivity than the matrix, and that the pressure is continuous across the septa, i.e., $\hat{p} = 0$. As a result, continuous finite elements can be used for spatial discretization. Note that the assumption of continuous pressure can be relaxed to include discontinuous pressure across the septa (Capatina et al. 2016; Fumagalli and Scotti 2013). We additionally assume that the injection site is located in the tissue matrix, thus we obtain $q_\Gamma = 0$. The new model, for fluid flow and drug transport along the septa embedded in deformable porous tissue, is summarized as

$$w_d \frac{\partial \epsilon_{v,\Gamma}}{\partial t} + \nabla_\Gamma \cdot \boldsymbol{w}_\Gamma = \llbracket \boldsymbol{w} \cdot \boldsymbol{n} \rrbracket, \quad \text{on } \Gamma \times (0, T], \tag{16a}$$

$$\llbracket p \rrbracket = 0, \quad \text{on } \Gamma \times (0, T], \tag{16b}$$

$$w_d \frac{\partial}{\partial t}\left(\phi_\Gamma C_\Gamma\right) + \nabla_\Gamma \cdot \left(\boldsymbol{w}_\Gamma C_\Gamma \right) = \llbracket \boldsymbol{w} \cdot \boldsymbol{n} C^* \rrbracket, \quad \text{on } \Gamma \times (0, T]. \tag{16c}$$

Equations (8) and (16) together are the proposed MDMS poroelastic model for the adipose tissue. Equation () describes the poroelastic behavior and fluid transport of the macroscale tissue matrix, while Eq. (16) models the fluid flow and drug transport along the microscale septa.

3 Numerical methods

In this section, we briefly introduce the numerical methods, including temporal and spatial discretizations, and solution algorithms, used in this work. The numerical methods are implemented using the open-source finite element library `deal.II` (Arndt et al. 2020; Bangerth et al. 2007; Bause et al. 2017; Odsæter et al. 2019).

3.1 Temporal discretization

The implicit second-order backward differentiation formula, denoted as BDF_2, is adopted for temporal discretization. For a scalar function φ, we have

$$\frac{\partial \varphi}{\partial t} \approx BDF_2(\varphi^n) = \frac{1}{2\Delta t}\big(3\varphi^n - 4\varphi^{n-1} + \varphi^{n-2}\big), \qquad (17)$$

where $\Delta t = t^n - t^{n-1}$ is the uniform time step between time t^n and t^{n-1}, for $n \geq 1$, and $\varphi^n \approx \varphi(t^n)$.

3.2 Spatial discretization

We introduce next the spatial discretization. For the rest of the work, we limit ourselves to two dimensions, $d = 2$. Let $\mathcal{T}_h$, consisting of quadrilateral polygons, be a conforming, shape-regular, and quasi-uniform triangulation of Ω. We decompose the boundary $\partial\Omega$ into Dirichlet and Neumann boundaries as

$$\partial\Omega = \partial\Omega_D^{\boldsymbol{u}} \cup \partial\Omega_N^{\boldsymbol{u}} = \partial\Omega_D^p \cup \partial\Omega_N^p, \text{ and } \partial\Omega_D^{\boldsymbol{u}} \cap \partial\Omega_N^{\boldsymbol{u}} = \partial\Omega_D^p \cap \partial\Omega_N^p = \emptyset, \qquad (18)$$

where $\partial\Omega_D^{\boldsymbol{u}}$ and $\partial\Omega_N^{\boldsymbol{u}}$ are the Dirichlet and Neumann boundaries for solid displacement, while $\partial\Omega_D^p$ and $\partial\Omega_N^p$ are the Dirichlet and Neumann boundaries for pressure. We remark that drug can only enter or exit the tissue with the fluid. Thus, the boundary conditions for drug concentration follow the fluid velocity.

Following (Odsæter et al. 2019), we distinguish between $\mathcal{T}_h^S = \big\{K \in \mathcal{T}_h : K \cap \Gamma \neq \emptyset\big\}$ and $\mathcal{T}_h^M = \mathcal{T}_h \backslash \mathcal{T}_h^S$ as illustrated in Fig. 2b. Define $\mathcal{F}_h$ as the set of all element faces. Then, $\mathcal{F}_h$ can be divided into $\mathcal{F}_h = \mathcal{F}_{h,D} \cup \mathcal{F}_{h,N} \cup \mathcal{F}_{h,I}$ where $\mathcal{F}_{h,D} \cap \mathcal{F}_{h,N} \cap \mathcal{F}_{h,I} = \emptyset$. Herein, $\mathcal{F}_{h,D}$ and $\mathcal{F}_{h,N}$ are the element faces on the Dirichlet ($\partial\Omega_D^p$) and Neumann $\partial\Omega_N^p$ boundaries for pressure, respectively; $\mathcal{F}_{h,I}$ is the set of element faces that are in the interior of the domain. Moreover, we have

$\mathcal{F}_{h,I} = \mathcal{F}_{h,I}^S \cup \mathcal{F}_{h,I}^M$ as shown in Fig. 2b. In addition, we define the inner product on $\mathcal{T}_h$ and $\mathcal{F}_h$ respectively as

$$(\cdot, \cdot)_{\mathcal{T}_h} = \sum_{K \in \mathcal{T}_h} (\cdot, \cdot)_K, \quad (\cdot, \cdot)_{\mathcal{F}_h} = \sum_{F \in \mathcal{F}_h} (\cdot, \cdot)_F, \qquad (19)$$

where $(\cdot, \cdot)_O$ is the inner product over the object O which can be an element $K \in \mathcal{T}_h$, or an element face $F \in \mathcal{F}_h$.

3.2.1 Poroelastic equations

We adopt the Galerkin method for spatial discretization of the poroelastic model. More specifically, continuous Galerkin (CG) is used for the conservation of linear momentum and conservation of mass equations. The finite element spaces are defined as

$$\boldsymbol{V}_h := \Big\{ \boldsymbol{v}_h \in \big[H^1(\Omega)\big]^d : \boldsymbol{v}_h|_K \in \big[\mathbb{P}_1(K)\big]^d,$$
$$\forall K \in \mathcal{T}_h, \boldsymbol{v}_h|_{\partial\Omega_D^{\boldsymbol{u}}} = \boldsymbol{0} \Big\}, \qquad (20a)$$

$$Q_{1,h} := \big\{ \theta_h \in H^1(\Omega) : \theta_h|_K \in \mathbb{P}_1(K),$$
$$\forall K \in \mathcal{T}_h, \theta_h|_{\partial\Omega_D^p} = 0 \big\}, \qquad (20b)$$

where H^1 is the classical Sobolev space, and $\mathbb{P}_r$ denotes polynomials of order $r \geq 0$.

The weak form of the conservation of linear momentum Eq. (8a) is given as

$$\big(\boldsymbol{\sigma}(\boldsymbol{u}_h^n, p_h^n), \nabla\boldsymbol{v}_h\big)_{\mathcal{T}_h} = \big(\boldsymbol{\sigma}(\boldsymbol{u}_h^n, p_h^n)\cdot\boldsymbol{n}, \boldsymbol{v}_h\big)_{\partial\Omega_N^{\boldsymbol{u}}}, \quad \forall\boldsymbol{v}_h \in \boldsymbol{V}_h. \qquad (21)$$

Similarly, the weak form of the conservation of mass Eqs. (8b) and (16a) can be written as (Burman et al. 2019; Odsæter et al. 2019)

$$\big(BDF_2(\epsilon_v^n), \theta_h\big)_{\mathcal{T}_h} - \big(\boldsymbol{w}^n(p_h^n), \nabla\theta_h\big)_{\mathcal{T}_h}$$
$$+ \big(BDF_2(\epsilon_{v,\Gamma}^n)w_d, \theta_h\big)_{\Gamma\cap\mathcal{T}_h} - \big(\boldsymbol{w}_\Gamma^n(p_h^n), \nabla_\Gamma\theta_h\big)_{\Gamma\cap\mathcal{T}_h}$$
$$= \big(q_f, \theta_h\big)_{\mathcal{T}_h} - \big(w_N, \theta_h\big)_{\partial\Omega_N^p}$$
$$- \sum_{\boldsymbol{x}\in\Gamma\cap\partial\Omega_N^p} w_d w_N(\boldsymbol{x})\theta_h(\boldsymbol{x}), \quad \forall\theta_h \in Q_{1,h}. \qquad (22)$$

where w_N is the boundary data for Darcy velocity, and we have used the following notations $\epsilon_v^n = \epsilon_v(\boldsymbol{u}_h^n), \epsilon_{v,\Gamma}^n = \epsilon_{v,\Gamma}(\boldsymbol{u}_h^n)$.

3.2.2 Darcy velocity approximation

Before presenting the weak form of the transport Eqs. (8c) and (16c), we need to calculate the discrete Darcy velocity $\boldsymbol{w}$ and $\boldsymbol{w}_\Gamma$. Because the discrete pressure field is only

piece-wise continuous, we instead take the average of the velocity across an element face as follows:

$$
W_h^n = \begin{cases} -\mathcal{K}_e \{\!\{ \nabla p_h^n \cdot \boldsymbol{n}_F \}\!\}, & \text{on } F \in \mathcal{F}_h \backslash \left(\mathcal{F}_{h,\mathrm{I}}^{\mathrm{S}} \cup \mathcal{F}_{h,\mathrm{N}} \right), \\ -\frac{1}{|F|} \{\!\{ \kappa_\Gamma \nabla_\Gamma p_h^n \cdot \boldsymbol{t}_\Gamma \}\!\}, & \text{on } F \in \mathcal{F}_{h,\mathrm{I}}^{\mathrm{S}}, \\ w_{\mathrm{N}}, & \text{on } F \in \mathcal{F}_{h,\mathrm{N}}, \end{cases}
$$

$$(23)$$

where $\mathcal{K}_e = \frac{2\mathcal{K}_+ \mathcal{K}_-}{\mathcal{K}_+ + \mathcal{K}_-}$ is the harmonic average of the hydraulic conductivity $\mathcal{K}$ of the element K at the element face $F \subset K$. More specifically, $\mathcal{K} = \mathcal{K}_m$ if $K \in \mathcal{T}_h^{\mathrm{M}}$, and $\mathcal{K} = \mathcal{K}_\Gamma$ if $K \in \mathcal{T}_h^{\mathrm{S}}$. Additionally, in Eq. (23), $\boldsymbol{n}_F$ is the unit vector outward normal of F, $|(\cdot)|$ denotes the measure of $(\cdot)$, and for a scalar function φ, $\{\!\{ \cdot \}\!\}$ is the arithmetic average operator

$$
\{\!\{ \varphi \}\!\} = \frac{1}{2} \left(\varphi_+ + \varphi_- \right). \tag{24}
$$

We remark that in Eq. (23) for $F \in \mathcal{F}_{h,\mathrm{I}}^{\mathrm{S}}$, we have used the following approximation $W_h^n|_F \approx W_h^n|_{F \cap \Gamma}$ because $W_h^n|_{F \backslash \Gamma} \ll W_h^n|_{F \cap \Gamma}$.

It is well-known that Eq. (23) obtained using piece-wise continuous approximation of the pressure field is not locally mass-conservative, and that applying Eq. (23) in conjunction with the DG method to the transport equation leads to artificial source and sink terms (Kadeethum et al. 2021; Sun and Wheeler 2006). A common resolution is to postprocess W_h^n as follows:

$$
V_h^n = \begin{cases} W_h^n + \mathcal{K}_e [\![y^n]\!], & \text{on } F \in \mathcal{F}_h \backslash \mathcal{F}_{h,\mathrm{N}}, \\ w_{\mathrm{N}}, & \text{on } F \in \mathcal{F}_{h,\mathrm{N}}, \end{cases} \tag{25}
$$

which is continuous across element faces, and satisfies the local mass conservation condition on each element. In Eq. (25), $y^n \in Q_{0,h}$ is the unique solution of the following equation (Odsæter et al. 2017)

$$
\left(\mathcal{K}_e [\![y^n]\!], [\![z]\!] \right)_{\mathcal{F}_h \backslash \mathcal{F}_{h,\mathrm{N}}} = \left(\mathcal{R}(W_h^n), z \right)_{\mathcal{T}_h}, \forall z \in Q_{0,h}, \tag{26}
$$

where

$$
Q_{0,h} := \left\{ \psi_h \in L^2(\Omega) : \psi_h|_K \in \mathbb{P}_0(K), \forall K \in \mathcal{T}_h, \right\}, \tag{27}
$$

is the classical Lebesgue space,

$$
\mathcal{R}(W_h^n)|_K = \begin{cases} \frac{1}{|K|} \left(\int_K \left(q_f - \mathrm{BDF}_2(\epsilon_v^n) \right) \mathrm{d}V - \int_{\partial K} W_h^n \boldsymbol{n}_F \cdot \boldsymbol{n}_K \mathrm{d}S \right), & K \in \mathcal{T}_h^{\mathrm{M}}, \\ \frac{1}{|K|} \left(\int_{K \cap \Gamma} \left(-\mathrm{BDF}_2(\epsilon_{v,\Gamma}^n) w_d \right) \mathrm{d}S - \int_{\partial K} W_h^n \boldsymbol{n}_F \cdot \boldsymbol{n}_K \mathrm{d}S \right), & K \in \mathcal{T}_h^{\mathrm{S}}, \end{cases} \tag{28}
$$

is the residual of the equation of conservation of mass, and measures the flux discrepancy from local mass conservation. In Eq. (28), $\boldsymbol{n}_K$ in the unit vector outward normal of the element K.

3.2.3 Transport equations

Finally, we are ready to present the weak form of the transport equations. Because the transport equations (8c) and (16c) are convection-dominated problems (Kadeethum et al. 2021; Rudraraju et al. 2013; Tran and Jha 2020), continuous Galerkin methods and central finite difference methods result into oscillations of the concentration field. It is necessary to use advanced numerical methods as in Brooks and Hughes (1982), Hughes et al. (1989) and Leng et al. (2022). We use the discontinuous Galerkin (DG) method with upwind scheme to ensure numerical stability. Thus, we did not observe any numerical instabilities of the concentration field. As discussed in Odsæter et al. (2019), the zeroth-order DG method is equivalent to the finite volume method. Thus, we present the finite volume formulation for the transport equations for simplicity,

$$
\sum_{K \in \mathcal{T}_h^{\mathrm{M}}} \int_K \mathrm{BDF}_2(\phi^n C_h^n) \mathrm{d}V + \sum_{K \in \mathcal{T}_h^{\mathrm{S}}} \int_{K \cap \Gamma} \mathrm{BDF}_2(\phi_\Gamma^n C_h^n) w_d \, \mathrm{d}S
$$
$$
+ \sum_{K \in \mathcal{T}_h} \int_{\partial K} V_h^n C_h^n \boldsymbol{n}_K \cdot \boldsymbol{n}_F \, \mathrm{d}S = \sum_{K \in \mathcal{T}_h} \int_K q_f \, \mathrm{d}V. \tag{29}
$$

To derive Eq. (29), we have used the approximation

$$
\int_{K \cap \Gamma} [\![\boldsymbol{w} \cdot \boldsymbol{n} C_h^*]\!] \mathrm{d}S \approx \sum_{\hat{K} \in \mathcal{T}_h^{\mathrm{M}}} \int_{\partial \hat{K} \cap \partial K} \boldsymbol{w} \cdot \boldsymbol{n} C_h \mathrm{d}S, \tag{30}
$$

and more details can be found in Odsæter et al. (2019). It is worth noting that for $K \in \mathcal{T}_h^{\mathrm{M}}$, we have let C_h be the drug concentration in the tissue matrix; for $K \in \mathcal{T}_h^{\mathrm{S}}$, we have let C_h represent the drug concentration in the septa.

3.3 Solution algorithm

The fixed-stress splitting algorithm solves the poroelastic equations sequentially (Kim et al. 2009, 2011), thus it allows the use of different numerical methods and preconditioners for the conservation of linear momentum Eq. (8a) and conservation of mass Eq. (8b). Because the poroelastic and transport models are weakly coupled, we apply the fixed-stress splitting algorithm to solve the linear poroelastic model Eqs. (21) and (22). After obtaining the solid displacement and pore pressure, we proceed to solve the transport equation (29). A similar solution algorithm can be found in Kadeethum et al. (2021) and Tran and Jha (2020). The solution algorithm is summarized in Algorithm 1.

Algorithm 1: Solution algorithm

Initialize $\boldsymbol{u}_h^0$, p_h^0, C_h^0.

At each time t^n, for $n \geq 1$,

    Solve the linear poroelastic model using the fixed-stress split algorithm.

    Repeat:

        Solve the conservation of mass, eq. (22).

        Solve the conservation of momentum, eq. (21).

    Until convergence.

    Obtain $\boldsymbol{u}_h^n$ and p_h^n.

    Update flux on element faces by solving eq. (26), and obtain V_h^n from eqs. (23) and (25).

    Solve the transport equation (29), and obtain C_h^n.

Increment $t^n \to t^{n+1}$.

---

4 Model verification

In this section, we verify the MDMS poroelastic model, Eqs. (8) and (16), by comparing simulation results against the full 2D model, Eq. (8) for $d = 2$, where the septa are resolved using fine meshes. We focus on the vertical plane that is perpendicular to the skin surface, and assume plane strain condition.

Taking $\Omega = (0, 0.01 \text{ m})^2$, see Fig. 3a, we assume there are six septa inside the tissue. If not stated otherwise, the units for length and position are meter (m) and are omitted for the rest of the work. Following (Leng et al. 2021b), we choose the following model parameters of the tissue matrix $E = 10$ kPa, $v = 0.49$, $\phi_0 = 0.2$, $\mu_f = 1$ cP, and $k_m = 1 \times 10^{-14}$ m². In this verification example, the drug is injected uniformly from the left boundary, $x = 0$, thus we have $q_f = 0$. The fluid is free to flow out of the tissue sample from the right boundary, $x = 0.01$. The top surface of the tissue is subjected to compression. The boundary conditions are

$$\begin{cases} \nabla p \cdot \boldsymbol{n} = -w_{\text{N}}, \quad \boldsymbol{u} \cdot \boldsymbol{n} = 0, \left(\boldsymbol{\sigma}^{\text{eff}} \boldsymbol{n} \right) \cdot \boldsymbol{t} = 0, & \text{on } x = 0, \\ p = 0, \quad \boldsymbol{\sigma}^{\text{eff}} \boldsymbol{n} = \boldsymbol{0}, & \text{on } x = 0.01, \\ \nabla p \cdot \boldsymbol{n} = 0, \quad \boldsymbol{\sigma}^{\text{eff}} \boldsymbol{n} = \boldsymbol{0}, & \text{on } y = 0, \\ \nabla p \cdot \boldsymbol{n} = 0, \quad \boldsymbol{\sigma}^{\text{eff}} \boldsymbol{n} = \boldsymbol{T}, & \text{on } y = 0.01, \end{cases}$$
$$(31)$$

where $w_{\text{N}} = 0.01$ m/s, and $\boldsymbol{T} = [0, -1.0 \text{ Pa}]^T$. We impose the drug concentration $C = 1$ at the inflow boundary $x = 0$. Taking uniform time step $\Delta t = 0.00001$ s, we study the drug distribution in the tissue and along the septa at $t = 0.5$ s.

To verify the model, we assume that all the septa have the same constant width $w_d = 15.625 \, \mu\text{m}$ Comley and Fleck (2010). We assume additionally that the permeability along the septa is $k_\Gamma = 1 \times 10^{-9}$ m². We consider septa fibers that

are aligned with one of the Cartesian coordinates. It is worth nothing that the orientation of the septa in the MDMS model can be arbitrary. This assumption for septa orientation is for verification only. As a result, the septa can be resolved using fine meshes for the full 2D model. An adaptively refined coarse mesh is shown in Fig. 3b, which is the base for all mesh refinements. Three local mesh refinements near the septa are further shown in Fig. 3c–e. In Fig. 3c, the smallest mesh size, h, is twice as large as the septa width w_d. Figure 3d, e demonstrate mesh refinements for $h = w_d$ and $h = 0.5w_d$, respectively. As shown in Fig. 3c–e, we have used adaptively refined meshes in order to achieve more accurate solutions near the septa. Other similar techniques such as T-splines and B-Splines-based isogeometric analysis (Casquero et al. 2017, 2018) can also be applied to our proposed MDMS model.

We first solve the full 2D model, Eq. (8), using finest mesh refinements as shown in Fig. 3e. The solution of the full 2D model is regarded as reference solution because the septa are resolved explicitly using fine meshes. Then, we solve the proposed MDMS poroelastic model, Eqs. (8) and (16), using two mesh refinements presented in Fig. 3c, d, and compare numerical solutions against that of the full 2D model. The major interest of this work is to study the drug distribution in the tissue matrix and along the septa. For that reason, we present only the spatial distribution of drug concentration in the tissue at $t = 0.5$ s in Fig. 4, and discuss the pressure and vertical displacement in "Appendix". Figure 4 shows that the numerical solutions of the MDMS model agree with the reference solution both in the matrix and along the septa. To have a quantitative comparison of the drug transport along the septa, we further show the concentration along the six septa at $t = 0.5$ s in Fig. 5. We observe

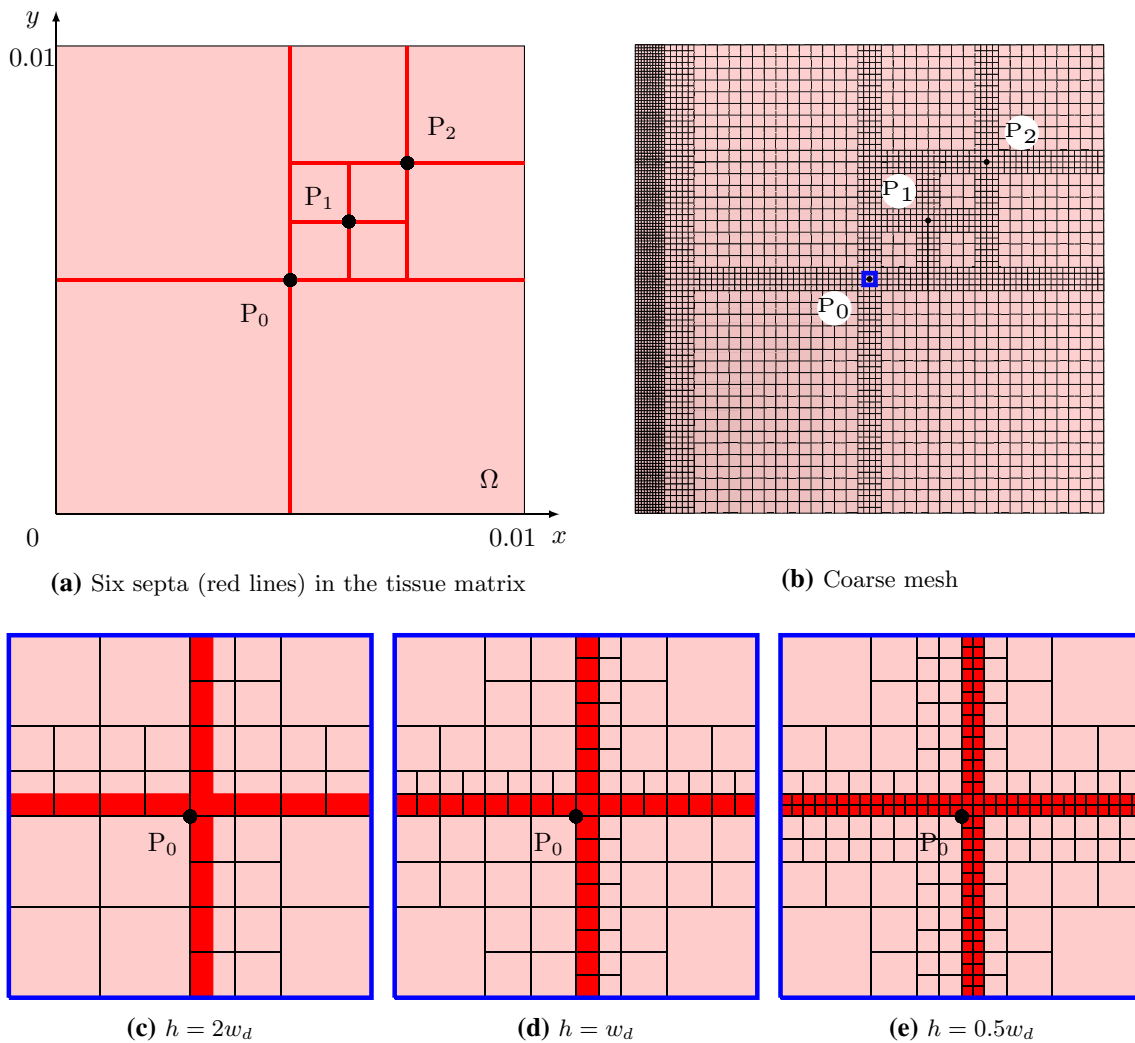**(a)** Six septa (red lines) in the tissue matrix

(b) Coarse mesh

(c) $h = 2w_d$

(d) $h = w_d$

(e) $h = 0.5w_d$

Fig. 3 The domain in (**a**) contains six septa. The mesh in (**b**) is adaptively refined along each septa as well as near the left boundary, $x = 0$. The mesh in the blue square is further shown in (**c–e**) for three different mesh refinements. The coordinates of the annotated points are P_0 (0.005, 0.005), P_1 (0.00625, 0.00625), and P_2 (0.0075, 0.0075). The septa width w_d is fixed. The smallest mesh element of each refinement is denoted as h. P_0 is shown in each figure as a reference to (**b**). Note that the mesh size near the left boundary $x = 0$ is the same as that along the septa

that drug concentration along each septa is in good agreement with the reference solution. In conclusion, the MDMS poroelastic model presented in Sect. 2.2 can capture the fluid flow and drug transport along the septa. Thus, this model is well-suited to study the fluid flow and poroelastic response of the tissue with embedded septa.

5 Application to subcutaneous injection

In this section, we apply the MDMS poroelastic model to study subcutaneous injection. Using symmetry, we can simplify the problem and perform simulation on the domain that is located on half of the vertical plane. We consider a skin tissue of size $\Omega = (0, 0.05 \text{ m})^2$. Unless otherwise stated, the

model parameters of the tissue matrix are the same as those in Sect. 4. The injection is modeled as a constant source term located at the element that includes the injection point A as shown in Fig. 2a. More details on injection modeling can be found in Leng et al. (2021a, 2021b). We choose an injection rate of $q_f = 0.4$ mL/s/m, and the duration of the injection is $T = 5$ s. The skin is divided into three layers, namely, dermis, subcutis, and muscle. We assume a rectangular septa network in the adipose layer as shown in Fig. 6a. According to Comley and Fleck (2010), the septa width, w_d, in porcine tissue ranges from 30 μm to 10 nm, and the inter-septa distance can be of several millimeters. Even though the maximum thickness can be of several hundred microns in width for healthy non-cellulite human adipose tissue (Hexsel et al. 2009; Macchi et al. 2010; Wang et al. 2011), we are
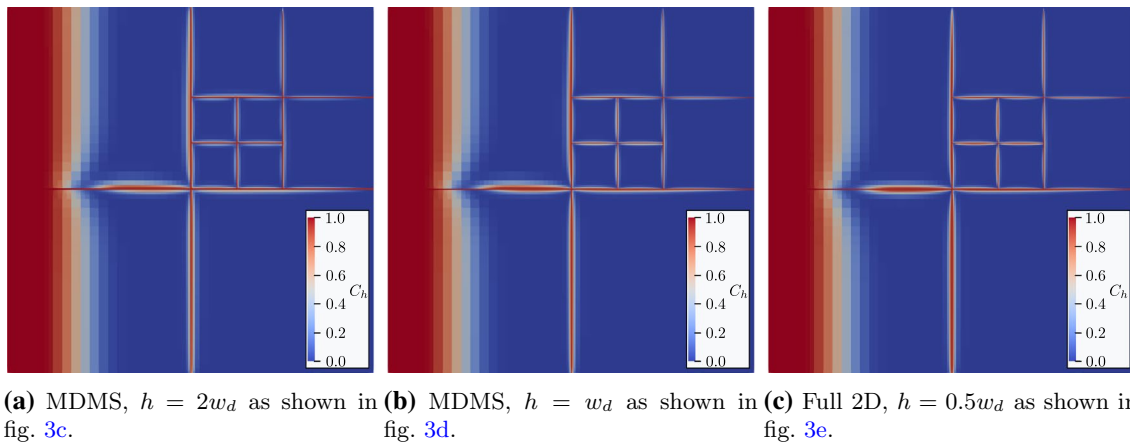
(a) MDMS, $h = 2w_d$ as shown in fig. 3c.

(b) MDMS, $h = w_d$ as shown in fig. 3d.

(c) Full 2D, $h = 0.5w_d$ as shown in fig. 3e.

Fig. 4 Spatial distribution of concentration C_h in the tissue and along the septa at $t = 0.5$ s for the MDMS and full 2D models with three mesh refinements shown in Fig. 3

interested in the contribution of these microscale septa to drug transport. Thus, we assume that all septa in Fig. 6a have the same constant width $w_d = 10 \, \mu\text{m}$, and the inter-septa distance is 1 mm.

The tissue is fixed in position at the bottom surface $y = 0$. The symmetry line is located at $x = 0$. The injection takes place at 4.5 mm below the skin surface on the symmetry line, i.e., point A in Fig. 6a. Fluid can exit the tissue from the bottom and right surfaces. In summary, the boundary conditions are given as

$$\begin{cases} \nabla p \cdot \boldsymbol{n} = 0, & \boldsymbol{u} \cdot \boldsymbol{n} = 0, \left(\boldsymbol{\sigma}^{\text{eff}} \boldsymbol{n} \right) \cdot \boldsymbol{t} = 0, & \text{on } x = 0, \\ p = 0, & \boldsymbol{\sigma}^{\text{eff}} \boldsymbol{n} = \boldsymbol{0}, & \text{on } x = 0.05, \\ p = 0, & \boldsymbol{u} = \boldsymbol{0}, & \text{on } y = 0, \\ \nabla p \cdot \boldsymbol{n} = 0, & \boldsymbol{\sigma}^{\text{eff}} \boldsymbol{n} = \boldsymbol{0}, & \text{on } y = 0.05. \end{cases}$$
(32)

We take the time step to be $\Delta t = 0.001$ s. Figure 6b shows the adopted adaptive mesh refinement. Therein, we only show the region where the mesh is adaptively refined, i.e., light pink region in Fig. 6b. The dark pink region in Fig. 6b is uniformly refined but the mesh is not shown. The mesh size in the uniformly refined region, $h = 0.00015625$ m, is the same as the smallest mesh size in the light pink region. As indicated in Fig. 6a, b, the mesh in the subcutis layer is fine and uniform, but the mesh size is still much larger than the septa width, $w_d = 10 \, \mu\text{m}$. There are no septa in the muscle layer which justifies the use of the coarse mesh.

The ultimate goal of studying subcutaneous injection is to predict drug uptake. Drug solutions composed of mAbs are absorbed mainly through lymphatics, and fibrous septa are prelymphatic pathways (Klein 2000; Ryan 1989). Therefore, it is critical to study drug distribution inside the septa network because drug inside the septa network indicates the amount of drug that is more likely to be absorbed by the lymphatics. For all these reasons, we define a metric

$$\frac{V_{\text{sep.}}}{V_{\text{inj.}}} \times 100\%,$$
(33)

where $V_{\text{sep.}}$ is the volume of drug residing in the septa network, and $V_{\text{inj.}}$ is the total injected drug volume. Equation (33) measures the fraction of injected drug that enters the septa network. Here, we study factors, such as permeability, septa width, inter-septa distance, and concentration-dependent drug viscosity, that change the volume fraction of drug inside the septa network.

We first study the effect of the permeability. Instead of limiting ourselves to the absolute value of k_m and k_Γ, we focus on the permeability ratio between the septa and the tissue matrix,

$$k_r = \frac{k_\Gamma}{k_m}.$$
(34)

By fixing $k_m = 1 \times 10^{-14} \, \text{m}^2$ and changing k_Γ, we investigate how the permeability ratio k_r changes the volume fraction of injected drug inside the septa network. As presented in Fig. 7a, if the permeability ratio is small, $k_r = 100$, less than 10% of the drug enters the septa. The volume fraction of the drug that enters the septa increases with k_r. However, there is no further increase in drug volume inside the septa when k_r is greater or equal to 100,000, where about 80% of injected drug occupies the septa at the end of the injection.

Next, we study the effect of septa width w_d on drug distribution. As shown in Fig. 7b, changing the septa width from 10 to 1 µm dramatically alters the volume fraction of the drug entering the septa network, namely, from 80 to 20% at the end of the injection. Septa width is directly related to the volume capacity of the septa network. When $w_d = 1 \, \mu\text{m}$, the volume fraction of the drug in the septa network increases initially to 40% at $t = 2$ s, then drops

(a) $y = 0.005$ m

(b) $x = 0.005$ m

(c) $y = 0.0075$ m

(d) $x = 0.0075$ m
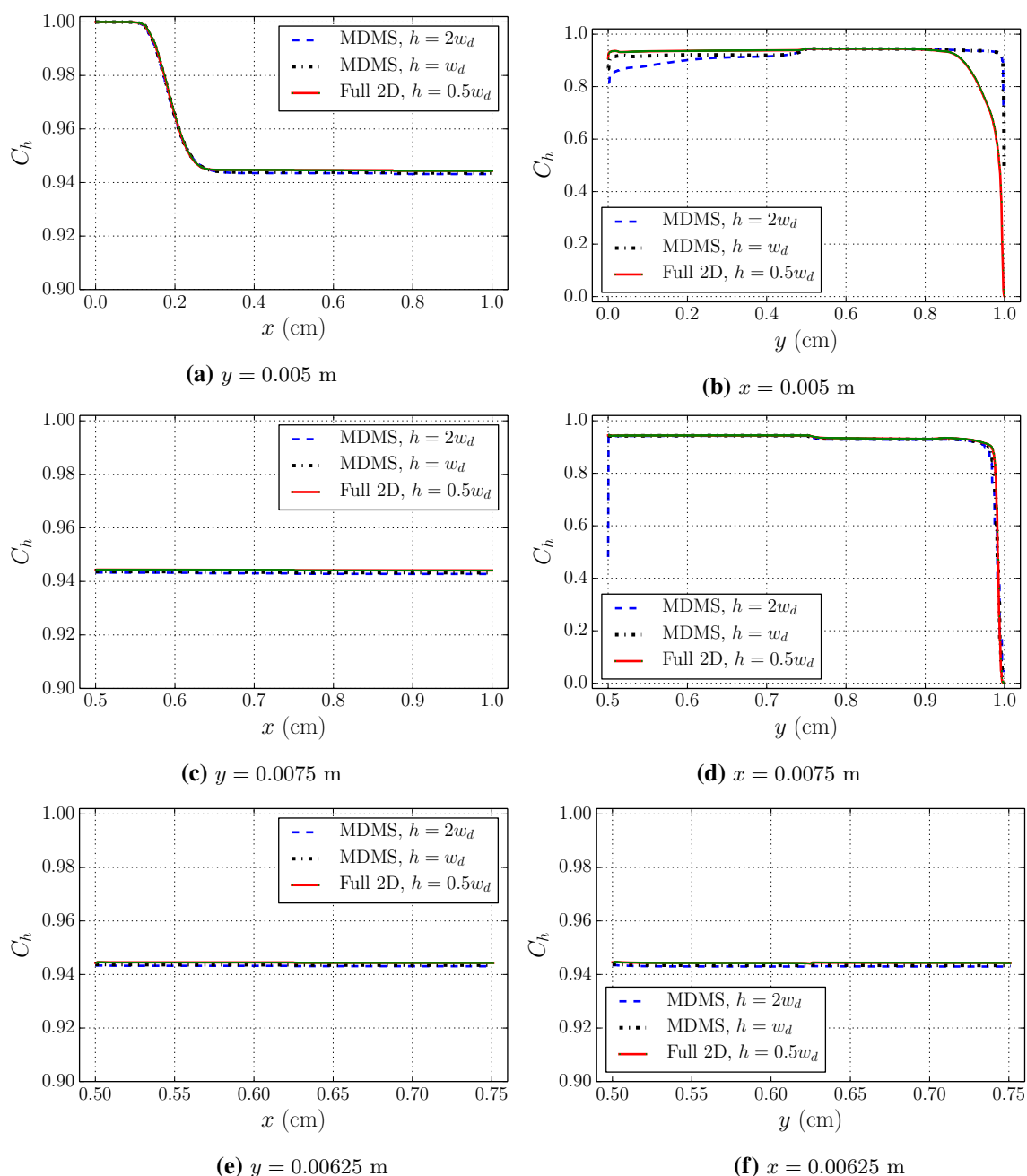
(e) $y = 0.00625$ m

(f) $x = 0.00625$ m

Fig. 5 Concentration along the six septa shown in Fig. 3a at $t = 0.5$ s for the MDMS and full 2D models with three mesh refinements presented in Fig. 3. For the full 2D model with mesh refinement as in Fig. 3e, $h = 0.5w_d$, the concentration is taken as the average across the width of the septa

to 20% at $t = 5$ s. This is due to the fact that the maximum volume capacity of the septa network is reached and later the drug travels from the septa to the matrix. This illustrates a non-trivial mechanism of drug transport whereby the drug can reach distant locations in the matrix traveling quickly through the septa and then going from the septa to the matrix.

Now, we study how the inter-septa distance affects drug distribution. First of all, we let the septa width be $w_d = 10\,\mu$m but change the inter-septa distance, denoted as $d_{\overline{w}}$, from 1 mm to 2 and 4 mm as shown in Fig. 8a. For a wider inter-septa distance $d_{\overline{w}}$, the total number of septa is reduced. As a result, the volume capacity of the septa network decreases. As shown in Fig. 9a, the volume

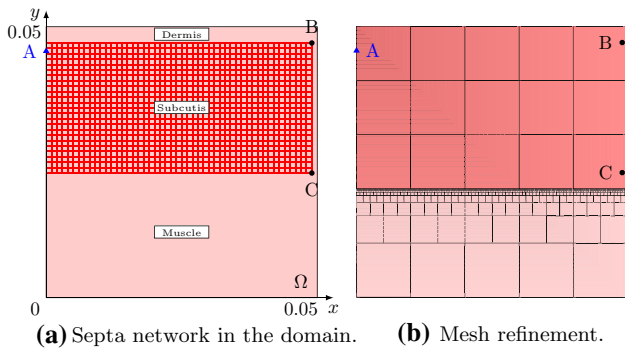**(a)** Septa network in the domain. **(b)** Mesh refinement.

Fig. 6 **a** A general septa network inside the subcuti layer of the skin. The coordinates of the three points are A (0, 0.0455), B (0.049, 0.047), and C (0.049, 0.023). The injection site is located at A. **b** The light pink region is adaptively refined. The dark pink region is uniformly refined (mesh not shown) and the mesh size is the same as the smallest mesh size, $h = 0.00015625$ m, in the light pink region

fraction of drug in the septa network drops significantly. Next, as in Fig. 8b, we change both the septa width w_d and inter-septa distance, denoted as d_w, so as to keep the volume capacity of the septa network approximately the

same. Even though the inter-septa distance is increased and there are fewer septa in the tissue, Fig. 9b indicates that the volume fraction of drug in the septa network does not vary much if the volume capacity of the septa network is kept constant.

Finally, we investigate the effect of concentration-dependent viscosity on drug distribution. We adopt the Ross-Minton equation to model the viscosity of the drug solution (Hung et al. 2019; Lilyestrom et al. 2013; Liu et al. 2005),

$$\mu_f(C) = \mu_{f0} \exp\left(\frac{v_i \widetilde{c}_0 C}{1 - v_i v_k \widetilde{c}_0 C}\right) \tag{35}$$

where $\mu_{f0} = 1$ cP is the viscosity of the interstitial fluid, $v_i = 0.0064$ mL/mg is the intrinsic viscosity, $v_k = 0.72$ depends on the crowding factor and shape determining factor. Equation (35) is illustrated in Fig. 10a for different initial mAbs concentration, $\widetilde{c}_0 = 1, 100, 120$ and 150 mg/mL. We remark that for concentration-dependent drug viscosity, the equations of conservation mass, Eqs. (8b) and (16a), become weakly coupled with the transport Eqs. (8c) and (16c). Following (Kadeethum et al. 2021; Tran and Jha 2020), we

Fig. 7 Effect of the permeability ratio, k_r, and septa width w on drug distribution. In (**a**), $w_d = 10\,\mu$m, $d_{\overline{w}} = 1$ mm, $\mu_f = 1$ cP. In (**b**), $k_r = 100,000$, $d_{\overline{w}} = 1$ mm, $\mu_f = 1$ cP. The gray shaded region indicates the duration of the injection

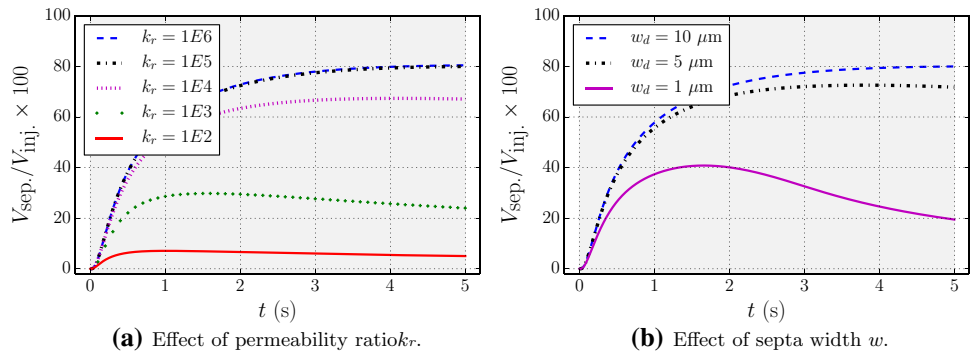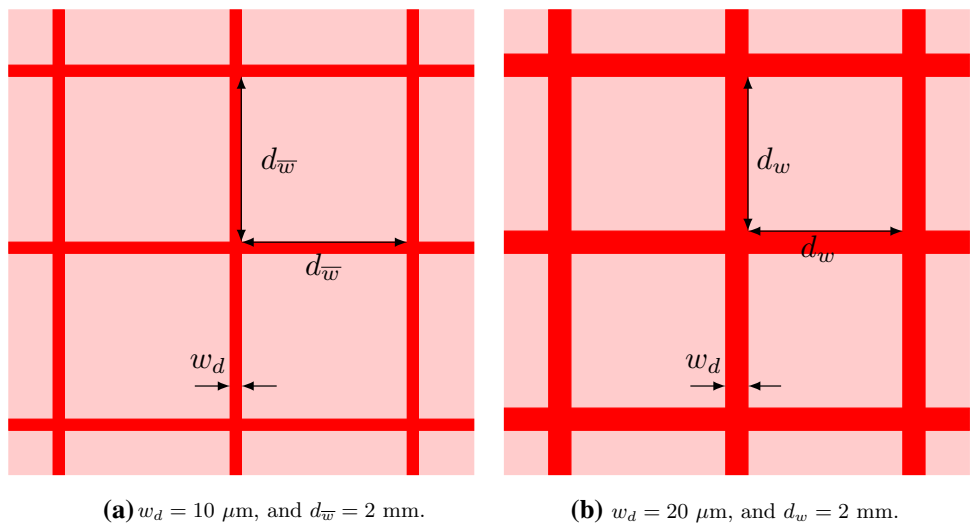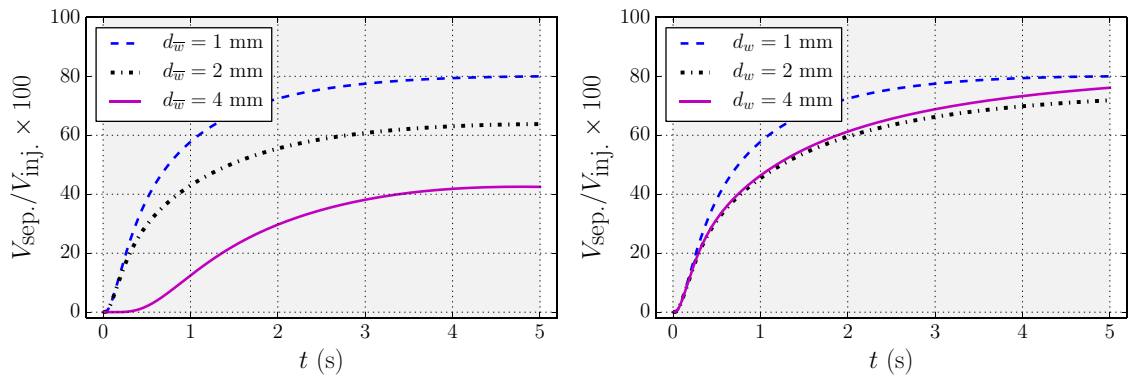**(a)** Effect of permeability ratio k_r. **(b)** Effect of septa width w.

Fig. 8 Red lines represent septa embedded in the tissue matrix. The width of the septa is exaggerated. **a** Change $d_{\overline{w}}$ only, w_d is kept constant. **b** Change d_w and w_d, keep the ratio d_w/w_d constant

(a) $w_d = 10\,\mu$m, and $d_{\overline{w}} = 2$ mm. **(b)** $w_d = 20\,\mu$m, and $d_w = 2$ mm.

(a) Change inter-septa distance and keep septa width constant.

(b) Change both the inter-septa distance and septa width.

Fig. 9 Effect of inter-septa distance on drug distribution. In (**a**), $k_r = 100{,}000$, $w_d = 10\,\mu$m, $\mu_f = 1$ cP. In (**b**), $k_r = 100{,}000$, $\mu_f = 1$ cP; and for $d_w = 1$ mm, $w_d = 10\,\mu$m; for $d_w = 2$ mm, $w_d = 20\,\mu$m; for $d_w = 4$ mm, $w = 40\,\mu$m. The gray shaded region indicates the duration of the injection
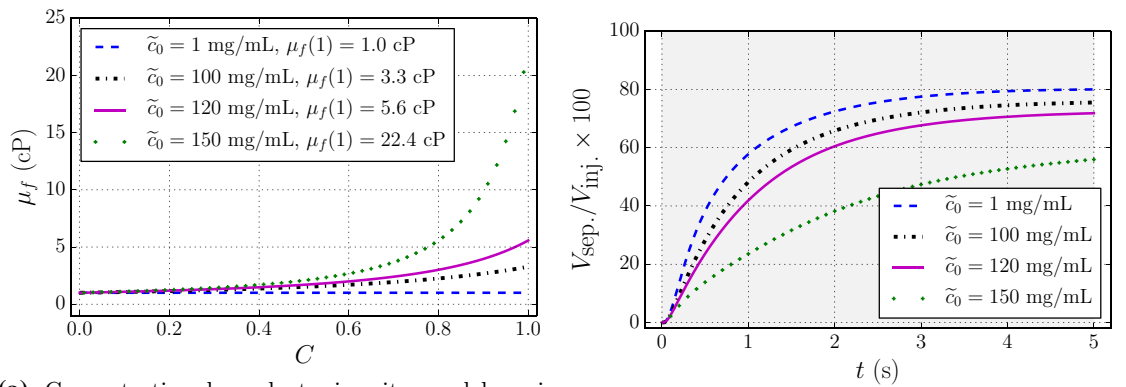
(a) Concentration-dependent viscosity model as in eq. (35).

(b) Effect of concentration-dependent viscosity.

Fig. 10 In (**a**), for $\widetilde{c}_0 = 1$ mg/mL, $\mu_f = 1$ cP is constant. In (**b**), $k_r = 100{,}000$, $w_d = 10\,\mu$m, $d_{\overline{w}} = 1$ mm. The gray shaded region in (**b**) indicates the duration of the injection

apply explicit coupling between concentration and viscosity to solve Eq. (22) by considering

$$\mu_f = \mu_f\left(\widetilde{C}_h^n\right), \text{ where } \widetilde{C}_h^n = 2C_h^{n-1} - C_h^{n-2}. \tag{36}$$

The mAbs concentration in the injected drug solution is gradually increased, and the drug viscosity grows exponentially. The volume fraction of drug inside the septa network is presented in Fig. 10b. When the initial mAbs concentration is increased from 1 to 120 mg/mL, the maximum drug

viscosity changes from 1 to 5.6 cP and the volume fraction of drug in the septa network is reduced by 10%. For high initial mAbs concentration, 150 mg/mL, the maximum drug viscosity becomes 22.4 cP and the volume fraction of the drug entering the septa network is decreased to 55%.

We have investigated numerically the effect of permeability, septa width, inter-septa distance and concentration-dependent viscosity on the drug distribution in the septa network as well as in the tissue matrix. These factors can be classified into two categories: flow resistance of the drug

and volume capacity of the septa network. Permeability and concentration-dependent drug viscosity correspond to the flow resistance of the drug, while septa width and inter-septa distance are closely related to the volume capacity of the septa network. Flow resistance of the drug determines the speed the injected drug can fill the septa network. The total volume of drug that can enter the septa network depends on the volume capacity of the septa network.

6 Conclusion

In this work, we have presented a mixed-dimensional multi-scale (MDMS) poroelastic model of adipose tissue for subcutaneous injection of mAbs. The tissue matrix is modeled as a homogeneous porous media. The fibrous septa are modeled explicitly as reduced-dimension microscale interfaces embedded in the macroscale tissue matrix. The MDMS poroelastic model is verified by comparing numerical results against the full 2D model where fibrous septa are resolved by fine meshes. Spatial distribution of drug concentration in the tissue and along the septa of the MDMS and full 2D models are in good agreement. More importantly, quantitative discrepancies of the drug concentration along each the septa obtained using the two models are negligible.

Then, we have applied the MDMS poroelastic model to study subcutaneous injection of mAbs. We found that the permeability ratio between the septa and tissue matrix, volume capacity of the septa network including septa width and inter-septa distance, and concentration-dependent drug viscosity are important factors affecting the amount of drug entering the septa network. Because septa constitute prelymphatic pathways, and mAbs are primarily absorbed by lymphatic capillaries, the results have important consequences for our understanding of mAbs uptake. Our model bridges the gap between existing computational approaches to mAb transport that assume isotropic, homogenized tissue properties and experiments which clearly show a preferential transport along septa. These embedded septa give rises to a highly anisotropic and heterogeneous drug distribution in the adipose tissue.

Our results also point to a previously overlooked mechanism of drug transport that enables quick migration of the drug from the injection site to distant locations of the tissue matrix. Our data show that the drug can travel far through the septa network. Then, if the septa that are distant to the injection size are filled with drug, the drug will migrate back from the septa to the tissue matrix.

Given the properties of the adipose tissue matrix and the studied injection conditions, this communication between distant locations in the tissue matrix is not possible without transport through the septa. The preferential transport of mAbs through confined spaces such as septa also highlights the importance of further studying the rheology of highly concentrated antibody solutions (Dandekar and Ardekani 2021).

In order to validate our MDMS model, subcutaneous injection experiments similar to those in Thomsen et al. (2014, 2015) should be conducted. One of the challenges for experiments is to measure drug concentration distribution in the tissue. Because mAbs have large molecular weight, small iodinated compounds, which are successfully used as contrast agents to track low molecular weight proteins (Comley and Fleck 2011; Thomsen et al. 2014, 2015), cannot be used to track mAbs. Fortunately, imaging techniques (He et al. 2020), such as positron emission tomography (Niu et al. 2009) and near-infrared fluorescence imaging (Cilliers et al. 2017), are promising in tracking mAbs distribution after subcutaneous injection.

This is the first step toward modeling fibrous septa using MDMS poroelastic models. In this work, we have assumed that the septa deformation is homogeneous as the tissue matrix. The next step is to model the solid deformation of the fibrous septa explicitly using similar ideas to those employed here for fluid flow. In addition, a simplified septa network is adopted. However, in actual adipose tissue each individual bundle of septa has its orientation, width, and length. For practical applications, it would be important to incorporate realistic septa characteristics from experiments for the study of subcutaneous injection. Finally, we have assumed the pressure is continuous thus have used continuous Galerkin for the pressure approximation. This assumption can be relaxed to consider a discontinuous pressure field. Thus, it is necessary to consider other numerical methods such as Capatina et al. (2016) and Fumagalli and Scotti (2013).

Appendix

Here, we provide additional data for the model verification presented in Sect. 4. We present spatial distributions of the vertical displacement u_y in Fig. 11 and pore pressure p in Fig. 12 using the MDMS and full 2D models with three mesh refinements.

(a) MDMS, $h = 2w_d$ as shown in fig. 3c.

(b) MDMS, , $h = w_d$ as shown in fig. 3d.

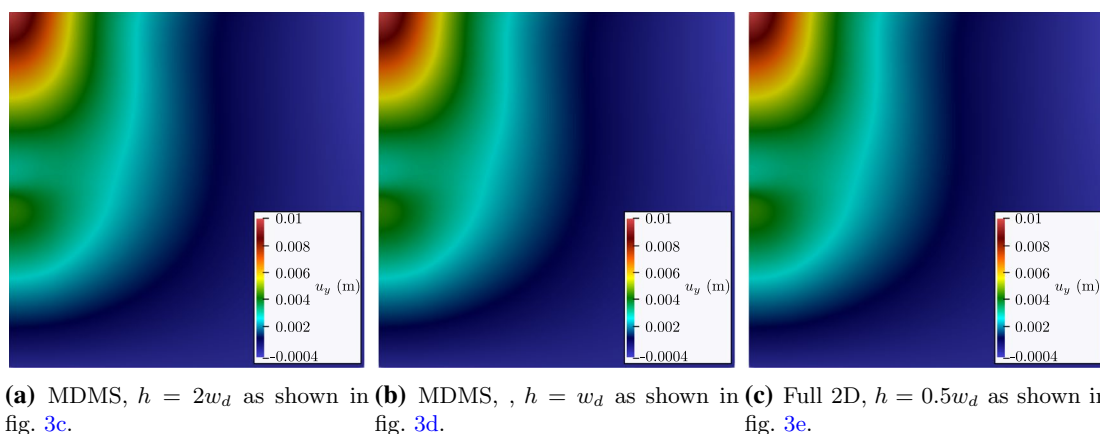**(c)** Full 2D, $h = 0.5w_d$ as shown in fig. 3e.

Fig. 11 Spatial distribution of vertical displacement $u_{y,h}$ in the tissue and along the septa at $t = 0.5$ s for the MDMS and full 2D models with three mesh refinements shown in Fig. 3
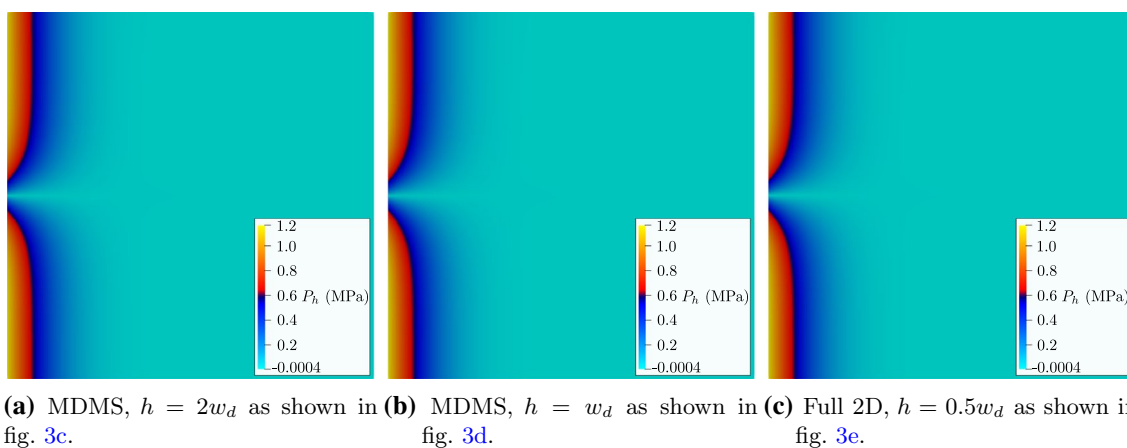

(a) MDMS, $h = 2w_d$ as shown in fig. 3c.

(b) MDMS, $h = w_d$ as shown in fig. 3d.

(c) Full 2D, $h = 0.5w_d$ as shown in fig. 3e.

Fig. 12 Spatial distribution of pressure p_h in the tissue and along the septa at $t = 0.5$ s for the MDMS and full 2D models with three mesh refinements shown in Fig. 3

References

Alboin C, Jaffré J, Roberts JE, Wang X, Serres C (2000) Domain decomposition for some transmission problems in flow in porous media. In: Numerical treatment of multiphase flows in porous media. Springer, pp 22–34

Angot P, Boyer F, Hubert F (2009) Asymptotic and numerical modelling of flows in fractured porous media. ESAIM Math Model Numer Anal 43(2):239–275

Arndt D, Bangerth W, Blais B, Clevenger TC, Fehling M, Grayver AV, Heister T, Heltai L, Kronbichler M, Maier M, Munch P, Pelteret J-P, Rastak R, Thomas I, Turcksin B, Wang Z, Wells D (2020) The deal.II library, version 9.2. J Numer Math 28(3):131–146

Bangerth W, Hartmann R, Kanschat G (2007) deal.II—a general purpose object oriented finite element library. ACM Trans Math Softw 33(4):24/1-24/27

Bause M, Radu FA, Köcher U (2017) Space-time finite element approximation of the biot poroelasticity system with iterative coupling. Comput Methods Appl Mech Eng 320:745–768

Biot MA (1941) General theory of three-dimensional consolidation. J Appl Phys 12(2):155–164

Biot MA (1956) Theory of propagation of elastic waves in a fluid-saturated porous solid. II. Higher frequency range. J Acoust Soc Am 28(2):179–191

Biot MA, Temple G (1972) Theory of finite deformations of porous solids. Indiana Univ Math J 21(7):597–620

Bittner B, Richter W, Schmidt J (2018) Subcutaneous administration of biotherapeutics: an overview of current challenges and opportunities. BioDrugs 32(5):425–440

Brooks AN, Hughes TJ (1982) Streamline upwind/Petrov-Galerkin formulations for convection dominated flows with particular emphasis on the incompressible navier-stokes equations. Comput Methods Appl Mech Eng 32(1–3):199–259

Burman E, Hansbo P, Larson MG (2019) A simple finite element method for elliptic bulk problems with embedded surfaces. Comput Geosci 23(1):189–199

Burmester GR, Panaccione R, Gordon KB, McIlraith MJ, Lacerda AP (2013) Adalimumab: long-term safety in 23 458 patients from global clinical trials in rheumatoid arthritis, juvenile idiopathic arthritis, ankylosing spondylitis, psoriatic arthritis, psoriasis and crohn's disease. Ann Rheum Dis 72(4):517–524

Capatina D, Luce R, El-Otmany H, Barrau N (2016) Nitsche's extended finite element method for a fracture model in porous media. Appl Anal 95(10):2224–2242

Casquero H, Liu L, Zhang Y, Reali A, Kiendl J, Gomez H (2017) Arbitrary-degree t-splines for isogeometric analysis of fully nonlinear Kirchhoff–Love shells. Comput Aided Des 82:140–153

Casquero H, Zhang YJ, Bona-Casas C, Dalcin L, Gomez H (2018) Non-body-fitted fluid–structure interaction: divergence-conforming b-splines, fully-implicit dynamics, and variational formulation. J Comput Phys 374:625–653

Cilliers C, Nessler I, Christodolu N, Thurber GM (2017) Tracking antibody distribution with near-infrared fluorescent dyes: impact of dye structure and degree of labeling on plasma clearance. Mol Pharm 14(5):1623–1633

Comley K, Fleck NA (2010) A micromechanical model for the Young's modulus of adipose tissue. Int J Solids Struct 47(21):2982–2990

Comley K, Fleck N (2011) Deep penetration and liquid injection into adipose tissue. J Mech Mater Struct 6(1):127–140

Coussy O (2004) Poromechanics. Wiley

Dandekar R, Ardekani AM (2021) New model to predict the concentration-dependent viscosity of monoclonal antibody solutions. Mol Pharm 18(12):4385–4392

de Lucio M, Bures M, Ardekani AM, Vlachos PP, Gomez H (2020) Isogeometric analysis of subcutaneous injection of monoclonal antibodies. Comput Methods Appl Mech Eng 373:113550

Faille I, Fumagalli A, Jaffré J, Roberts JE (2016) Model reduction and discretization using hybrid finite volumes for flow in porous media containing faults. Comput Geosci 20(2):317–339

Flemisch B, Berre I, Boon W, Fumagalli A, Schwenck N, Scotti A, Stefansson I, Tatomir A (2018) Benchmarks for single-phase flow in fractured porous media. Adv Water Resour 111:239–258

Fornells P, García-Aznar JM, Doblaré M (2007) A finite element dual porosity approach to model deformation-induced fluid flow in cortical bone. Ann Biomed Eng 35(10):1687–1698

Frih N, Martin V, Roberts JE, Saâda A (2012) Modeling fractures as interfaces with nonmatching grids. Comput Geosci 16(4):1043–1060

Froeschl P (2003) Fluid flow and transport in porous media: mathematical and numerical treatment. Am Math Mon 110(7):660

Fumagalli A, Scotti A (2013) A reduced model for flow and transport in fractured porous media with non-matching grids. In: Numerical mathematics and advanced applications 2011. Springer, pp 499–507

Glassman PM, Balthasar JP (2014) Mechanistic considerations for the use of monoclonal antibodies for cancer therapy. Cancer Biol Med 11(1):20

Haller MF (2007) Converting intravenous dosing to subcutaneous dosing with recombinant human hyaluronidase. Pharm Tech 31:861–864

Han D, Rahimi E, Aramideh S, Ardekani AM (2021) Transport and lymphatic uptake of biotherapeutics through subcutaneous injection. J Pharm Sci 111:752–768

He K, Zeng S, Qian L (2020) Recent progress in the molecular imaging of therapeutic monoclonal antibodies. J Pharm Anal 10(5):397–413

Hexsel DM, Abreu M, Rodrigues TC, Soirefmann M, do Prado DZ, Gamboa MML (2009) Side-by-side comparison of areas with and without cellulite depressions using magnetic resonance imaging. Dermatol Surg 35(10):1471–1477

Hossain SS, Kopacz AM, Zhang Y, Lee S-Y, Lee T-R, Ferrari M, Hughes TJ, Liu WK, Decuzzi P (2013) Multiscale modeling for the vascular transport of nanoparticles. In: Nano and cell mechanics: fundamentals and frontiers, pp 437–459

Hughes TJ, Franca LP, Hulbert GM (1989) A new finite element formulation for computational fluid dynamics: VIII. The Galerkin/least-squares method for advective-diffusive equations. Comput Methods Appl Mech Eng 73(2):173–189

Hung JJ, Zeno WF, Chowdhury AA, Dear BJ, Ramachandran K, Nieto MP, Shay TY, Karouta CA, Hayden CC, Cheung JK et al (2019) Self-diffusion of a highly concentrated monoclonal antibody by fluorescence correlation spectroscopy: insight into protein-protein interactions and self-association. Soft Matter 15(33):6660–6676

Jackisch C, Müller V, Maintz C, Hell S, Ataseven B (2014) Subcutaneous administration of monoclonal antibodies in oncology. Geburtshilfe Frauenheilkd 74(4):343

Kadeethum T, Lee S, Ballarin F, Choo J, Nick HM (2021) A locally conservative mixed finite element framework for coupled hydro-mechanical-chemical processes in heterogeneous porous media. Comput Geosci 152:104774

Kim J, Tchelepi HA, Juanes R et al (2009) Stability, accuracy and efficiency of sequential methods for coupled flow and geomechanics. In: SPE reservoir simulation symposium. Society of Petroleum Engineers

Kim J, Tchelepi HA, Juanes R (2011) Stability and convergence of sequential methods for coupled flow and geomechanics: fixed-stress and fixed-strain splits. Comput Methods Appl Mech Eng 200(13–16):1591–1606

Klein JA (2000) Tumescent technique: tumescent anesthesia & microcannular liposuction. Mosby Incorporated

Leng Y, Ardekani A, Gomez H (2021a) A poro-viscoelastic model for the subcutaneous injection of monoclonal antibodies. J Mech Phys Solids 155:104537

Leng Y, de Lucio M, Gomez H (2021b) Using poro-elasticity to model the large deformation of tissue during subcutaneous injection. Comput Methods Appl Mech Eng 384:113919

Leng Y, Tian X, Demkowicz L, Gomez H, Foster JT (2022) A Petrov-Galerkin method for nonlocal convection-dominated diffusion problems. J Comput Phys 452:110919

Lilyestrom WG, Yadav S, Shire SJ, Scherer TM (2013) Monoclonal antibody self-association, cluster formation, and rheology at high concentrations. J Phys Chem B 117(21):6373–6384

Liu J, Nguyen MD, Andya JD, Shire SJ (2005) Reversible self-association increases the viscosity of a concentrated monoclonal antibody in aqueous solution. J Pharm Sci 94(9):1928–1940

Lu R-M, Hwang Y-C, Liu I-J, Lee C-C, Tsai H-Z, Li H-J, Wu H-C (2020) Development of therapeutic antibodies for the treatment of diseases. J Biomed Sci 27(1):1–30

Macchi V, Tiengo C, Porzionato A, Stecco C, Vigato E, Parenti A, Azzena B, Weiglein A, Mazzoleni F, De Caro R (2010) Histotopographic study of the fibroadipose connective cheek system. Cells Tissues Organs 191(1):47–56

Martin V, Jaffré J, Roberts JE (2005) Modeling fractures and barriers as interfaces for flow in porous media. SIAM J Sci Comput 26(5):1667–1691

NíAnnaidh A, Bruyère K, Destrade M, Gilchrist MD, Maurini C, Otténio M, Saccomandi G (2012) Automated estimation of collagen fibre dispersion in the dermis and its contribution to the anisotropic behaviour of skin. Ann Biomed Eng 40(8):1666–1678

Niu G, Li Z, Xie J, Le Q-T, Chen X (2009) Pet of EGFR antibody distribution in head and neck squamous cell carcinoma models. J Nucl Med 50(7):1116–1123

Odsæter LH, Wheeler MF, Kvamsdal T, Larson MG (2017) Postprocessing of non-conservative flux for compatibility with transport in heterogeneous media. Comput Methods Appl Mech Eng 315:799–830

Odsæter LH, Kvamsdal T, Larson MG (2019) A simple embedded discrete fracture-matrix model for a coupled flow and transport

problem in porous media. Comput Methods Appl Mech Eng 343:572–601

Pivot X, Gligorov J, Müller V, Curigliano G, Knoop A, Verma S, Jenkins V, Scotto N, Osborne S, Fallowfield L et al (2014) Patients' preferences for subcutaneous trastuzumab versus conventional intravenous infusion for the adjuvant treatment of her2-positive early breast cancer: final analysis of 488 patients in the international, randomized, two-cohort prefher study. Ann Oncol 25(10):1979–1987

Porter CJ, Charman SA (2000) Lymphatic transport of proteins after subcutaneous administration. J Pharm Sci 89(3):297–310

Porter C, Edwards G, Charman SA (2001) Lymphatic transport of proteins after sc injection: implications of animal model selection. Adv Drug Deliv Rev 50(1–2):157–171

Rahimi E, Aramideh S, Han D, Gomez H, Ardekani AM (2022) Transport and lymphatic uptake of monoclonal antibodies after subcutaneous injection. Microvasc Res 139:104228

Rudraraju S, Mills KL, Kemkemer R, Garikipati K (2013) Multiphysics modeling of reactions, mass transport and mechanics of tumor growth. In: Computer models in biomechanics. Springer, pp 293–303

Ryan TJ (1989) Structure and function of lymphatics. J Investig Dermatol 93(2):S18–S24

Schädle P, Zulian P, Vogler D, Bhopalam SR, Nestola MG, Ebigbo A, Krause R, Saar MO (2019) 3d non-conforming mesh model for flow in fractured porous media using Lagrange multipliers. Comput Geosci 132:42–55

Schwenck N, Flemisch B, Helmig R, Wohlmuth BI (2015) Dimensionally reduced flow models in fractured porous media: crossings and boundaries. Comput Geosci 19(6):1219–1230

Shpilberg O, Jackisch C (2013) Subcutaneous administration of rituximab (mabthera) and trastuzumab (herceptin) using hyaluronidase. Br J Cancer 109(6):1556–1561

Skobe M, Detmar M (2000) Structure, function, and molecular control of the skin lymphatic system. J Investig Dermatol Symp Proc 5:14–19

Sommer G, Eder M, Kovacs L, Pathak H, Bonitz L, Mueller C, Regitnig P, Holzapfel GA (2013) Multiaxial mechanical properties and constitutive modeling of human adipose tissue: a basis for pre-operative simulations in plastic and reconstructive surgery. Acta Biomater 9(11):9036–9048

Sun S, Wheeler MF (2006) Projections of velocity data for the compatibility with transport. Comput Methods Appl Mech Eng 195(7–8):653–673

Supersaxo A, Hein WR, Steffen H (1990) Effect of molecular weight on the lymphatic absorption of water-soluble compounds following subcutaneous administration. Pharm Res 7(2):167–169

Taylor PC, Adams AC, Hufford MM, De La Torre I, Winthrop K, Gottlieb RL (2021) Neutralizing monoclonal antibodies for treatment of covid-19. Nat Rev Immunol 21(6):382–393

Thomas VA, Balthasar JP (2019) Understanding inter-individual variability in monoclonal antibody disposition. Antibodies 8(4):56

Thomsen M, Hernandez-Garcia A, Mathiesen J, Poulsen M, Sørensen DN, Tarnow L, Feidenhans R (2014) Model study of the pressure build-up during subcutaneous injection. PLoS ONE 9(8):e104054

Thomsen M, Rasmussen CH, Refsgaard HH, Pedersen K-M, Kirk RK, Poulsen M, Feidenhans R (2015) Spatial distribution of soluble insulin in pig subcutaneous tissue: effect of needle length, injection speed and injected volume. Eur J Pharm Sci 79:96–101

Tran M, Jha B (2020) Coupling between transport and geomechanics affects spreading and mixing during viscous fingering in deformable aquifers. Adv Water Resour 136:103485

Tso AR, Goadsby PJ (2017) Anti-CGRP monoclonal antibodies: the next era of migraine prevention? Curr Treat Options Neurol 19(8):1–11

Wang Y-N, Lee K, Ledoux WR (2011) Histomorphological evaluation of diabetic and non-diabetic plantar soft tissue. Foot Ankle Int 32(8):802–810

Wang W, Chen N, Shen X, Cunningham P, Fauty S, Michel K, Wang B, Hong X, Adreani C, Nunes CN et al (2012) Lymphatic transport and catabolism of therapeutic proteins after subcutaneous administration to rats and dogs. Drug Metab Dispos 40(5):952–962

Weickenmeier J, Mazza E (2019) Inverse methods. In: Skin biophysics. Springer, pp 193–213

Wright RT, Hayes D, Sherwood PJ, Stafford WF, Correia JJ (2018) AUC measurements of diffusion coefficients of monoclonal antibodies in the presence of human serum proteins. Eur Biophys J 47(7):709–722

Zhao L, Ji P, Li Z, Roy P, Sahajwalla CG (2013) The antibody drug absorption following subcutaneous or intramuscular administration and its mathematical description by coupling physiologically based absorption process with the conventional compartment pharmacokinetic model. J Clin Pharmacol 53(3):314–325